Available online at www.sciencedirect.com

ScienceDirect

journal homepage: www.elsevier.com/locate/he

Fe-doped ceria nanopowders synthesized by freeze-drying precursor method for electrocatalytic applications

Mariano O. Mazan [a], Jaasiel Marrero-Jerez [b,c], Analía Soldati [d], Pedro Núñez [b,c], Susana A. Larrondo [e,f,*]

[a] Departamento de Ingeniería Química, Facultad de Ingeniería, Universidad de Buenos Aires, Pabellón de Industrias, Ciudad Universitaria, 1428 Buenos Aires, Argentina
[b] Departamento de Química Inorgánica, Universidad de La Laguna, E-38200 La Laguna, Tenerife, Spain
[c] Instituto Universitario de Materiales y Nanotecnología, Universidad de La Laguna, E-38200 La Laguna, Tenerife, Spain
[d] CONICET, Caracterización de Materiales, Centro Atómico Bariloche, Instituto Balseiro, Av. Bustillo 9500, 8400 San Carlos de Bariloche, Rio Negro, Argentina
[e] Centro de Investigaciones en Sólidos CINSO-CITEDEF-UNIDEF-CONICET, J.B. de La Salle 4397, 1603 Pcia. Buenos Aires, Argentina
[f] Instituto de Investigación e Ingeniería Ambiental, Universidad Nacional de San Martín, UNSAM, Campus Miguelete, 25 de Mayo y Francia, 1650 San Martín, Provincia de Buenos Aires, Argentina

ARTICLE INFO

Article history:
Received 28 July 2014
Received in revised form
26 November 2014
Accepted 2 January 2015
Available online 11 February 2015

Keywords:
CeO_2–Fe_2O_3 solid solution
Nanoceramics
Freeze-drying
Enhanced reducibility
CO_2-TPD
Total conductivity

ABSTRACT

In this work iron doped ceria nanoceramics were successfully synthesized through the freeze-drying method. All the solids were nanocrystalline. The incorporation of iron reduced the crystallite size with the corresponding increment of specific surface area, favoured the sintering of the solids that could be achieved at lower temperatures, increased the reduction percentage achieved in hydrogen flow and increased the amount and strength of basic sites. The lattice parameter showed a continuous decrease with the increment in iron content indicating that iron was incorporated into fluorite ceria structure at concentrations above the solubility limit. Finally, the incorporation of iron improved the conductivity and reduced the activation energy of the process. The higher reducibility, the presence of basic sites and the higher conductivity position iron doped ceria materials as promising anodes for intermediate temperature SOFCs, operated with hydrocarbons.

* *Corresponding author*. Centro de Investigaciones en Sólidos CINSO-CITEDEF-UNIDEF-CONICET, J.B. de La Salle 4397, 1603 Pcia. Buenos Aires, Argentina. Tel.: +54 11 47098158.
E-mail addresses: slarrondo@citedef.gob.ar, slarrondo@unsam.edu.ar (S.A. Larrondo).
http://dx.doi.org/10.1016/j.ijhydene.2015.01.006

Introduction

The rapid increase in the consumption of fossil fuels for energy production has driven the research in the energy field to the development of new technologies with reduced environmental impact, the modification of existing technologies to use the fossil fuels more efficiently and the incorporation of hydrogen generated from biomass in the energy circuit [1].

In the area of development of new technologies with reduced environmental impact and high efficiency, fuel cells have occupied an important position. In particular, Solid Oxide Fuel Cells (SOFCs), consisted of a ceramic electrolyte with ionic conductivity by O^{2-} ion diffusion, are promising candidates for large distributed power generation for stationary applications (>100 kW), and also for small residential and very small scale portable power generation units (from 1 to 10 kW) [2]. One of the main advantages of SOFCs over the other types of fuel cells is their capacity for processing a variety of fuels like natural gas, light hydrocarbons, bioalcohols, and H_2-rich streams obtained from fossil fuels or biogas [2–11]. This type of fuel cells has a set of constitutive materials well established with good performance at high temperatures (>900 °C) [9–11]: Ytria Stabilized Zirconia (YSZ) as electrolyte, a nickel-electrolyte composite (Ni/YSZ "cermet") as anode and a Lanthanum Strontium Manganite (LSM) as cathode. The YSZ electrolyte restricts the operating temperature to the region of its good ionic conductivity: 0.1 S cm^{-1} at temperature above 900 °C. This high operating temperature leads to high costs and material degradation problems. Nowadays, the investigations are focused in the reduction of the operating temperature to the intermediate temperature range (500–700 °C) in order to make this technology economically feasible [5–10]. However, lowering the operating temperature reduces the kinetics of the processes that take place at the Three-Phase Boundary (TPB) on the electrodes surfaces, increasing the associated polarization resistance. One way to partially avoid this negative effect is the development of electrode materials with porous structure and mixed ionic and electronic conductivity, which allows the charge transfer reactions to take place, in principle, at the whole surface.

Many materials with different structures (spinel, pyrochloric, perovskite, etc.) have been tested as anodes. However, CeO_2-based materials with fluorite structure appear to be the most promising because their resistance to coke formation and sulphur poisoning and their ability to oxidize the carbon that may be formed in reactions with hydrocarbons [8–11]. Despite the good characteristics mentioned, these materials have poor electronic conductivity and morphological stability. It is well-known that doping with aliovalent cations leads to oxides with enhanced ionic conductivity due to the formation of oxygen ion vacancies. In this sense, Gd^{3+} with smaller ionic radius than that of cerium cation, has been intensively studied as ceria dopant specially as electrolyte material [12–15]. In recent years, many researchers have synthesized iron doped ceria solids for different catalytic and SOFCs applications [16–23]. It is very well-known that iron exhibits a very low solubility limit in ceria structure when solid state reaction is used as the synthesis process (<1 mol%) [24]. However, synthesis of nanomaterials can favour the solubility of larger amounts of iron thus increasing oxygen ion vacancies. The synthesis of Ce–Fe mixed oxides through mild processes yields very small particles in the nanoscale range. Nanostructured cerium oxides are expected to be good hosts for iron oxide and stabilize much more iron in solid solution than ceria composed of microscopic or larger crystals.

In this work, we present the synthesis and the characterization of nanosized $Ce_{1-x}Fe_xO_{2-\delta}$ mixed oxides, with x = 0, 0.1 and 0.2, by the freeze-drying precursor method, as possible materials for anodes of SOFCs of intermediate temperature. The effect of iron doping on the total conductivity of the resulting material is especially studied.

Materials and methods

Synthesis of nanostructured solids

The CeO_2–Fe_2O_3 solids were synthesized through the freeze-drying method with different atomic ratios (Fe/(Ce + Fe) = 0; 0.1 and 0.2). The samples were nominated according to their iron atomic content as 0Fe, 10Fe and 20Fe, respectively. The required amounts of $Ce(NO_3)_3 \cdot 6H_2O$ (Sigma–Aldrich, 99.99%) and $Fe(NO_3)_3 \cdot 9H_2O$ (Sigma–Aldrich, 99.99%) to obtain the desired compositions were individually dissolved in distilled water under magnetic stirring. EDTA (Sigma–Aldrich, 99.4%) was dissolved in an ammonia solution to be used as complexing agent, in a 1:1 ligand to metal molar ratio, to avoid precipitation. The pH of the solution, initially acid, was adjusted to 7–8 by adding aqueous ammonia. Droplets of the as-obtained solution were subsequently flash-frozen by pouring them into liquid nitrogen. Afterwards, the system was freeze-dried for 3 days (Heto freeze-dryer Lyolab 3000, Thermo Scientific, USA). The precursor was immediately calcined at 350 °C for 2 h with a heating ramp of 10 °C min^{-1}.

Characterization techniques

X-ray powder diffraction patterns (XPD, X'Pert Pro-automated diffractometer, PANalytical, USA) were acquired with a Bragg–Brentano configuration, a primary monochromator, CuKα_1 radiation and a X'Celerator detector, in the 10°–120° 2θ range. Rietveld refinements were performed for all the patterns using the Fullprof Suite software (Windows version, September 2012) [25]. Fluorite-type cubic structure was assumed (Fm3m space group) with Ce^{4+} and Fe^{3+} cations in 4a and O^{2-} anions in 8c positions; pseudo-Voigt peak shape was considered. The lattice parameters of the different samples were obtained from the refinements. Besides, crystallite sizes were estimated by applying the Scherrer equation (Eq. (1)) [26]:

$$D_{hkl} = \frac{0.9 \cdot \lambda}{\beta_{hkl} \cos \theta} \quad (1)$$

where D_{hkl} is the crystallite size obtained from the line broadening corresponding to the (hkl) Bragg peak, 0.9 is a shape constant, λ is the wavelength of the incident X-ray radiation, β_{hkl} is the width of Bragg peak at half maximum intensity after subtracting the instrumental contribution. The

(111) Bragg peak, which is the most intense in the fluorite-type structure, was selected for the crystallite size determination.

N_2-adsorption and desorption isotherms were obtained at (−196 °C) (Gemini 2365, Micromeritics, USA). The samples were previously degassed at 125 °C during 16 h. The Brunauer–Emmett–Teller (BET) method was used to calculate the specific surface area with the adsorption points corresponding to the 0.05–0.35 relative pressure range.

The morphology of the samples was examined by Scanning Electron Microscopy (SEM, Jeol JSM-6300, Japan) provided with Energy Dispersive X-ray Spectroscopy (EDS, D6699-ATW, Oxford Instruments, UK). High Resolution Transmission Electron Microscopy (HR-TEM, Philipps CM 200UT, The Netherlands) with ultra-twin lens and a LaB6 filament operated at 200 keV was used to get images in order to see grain sizes and their distribution. The instrument was also provided with a system to perform EDS (EDAX©) to analyse the chemical composition in different sample points. For TEM studies, samples were prepared by dispersing some milligrams of material in isopropyl alcohol by sonication during five minutes. A drop of the solution was transferred into a TEM copper grid coated with a carbon film and let dry in air.

Temperature Programmed Reduction with hydrogen (H_2-TPR, Autochem II 2920, Micromeritics, USA) was used to characterize the reducibility of the solids. Samples of 40 mg were degassed during one hour, with a 50 mL(STP) min^{-1} He flow, at 300 °C (heating ramp of 10 °C min^{-1}). After cooling down to room temperature, the reactor was heated up to 900 °C, at 10 °C min^{-1} in a 50 mL min^{-1} flow consisted of 5 mol % H_2 in Ar balance, while collecting the equipment output signal. The H_2 consumption and the percentage of reduction were calculated for each sample.

Carbon dioxide Temperature Programmed Desorption experiments (CO_2-TPD, Autochem II 2920, Micromeritics, USA) were also performed to study the relative strength of basic sites on solids surface. Samples of 100 mg were degassed during one hour, in a 50 mL (STP) min^{-1} He flow, at 300 °C (heating ramp of 10 °C min^{-1}). The system was cooling down to 30 °C and kept at this temperature during one hour. Afterwards, the reactor was purged with a 50 mL min^{-1} He flow during 90 min. Finally, the reactor was heated up to 900 °C, at 10 °C min^{-1}, with the same He flow while collecting the equipment output signal.

Preparation of sintered disks

In order to determine the overall conductivity of the synthesized materials it was necessary to prepare dense disks. The mixed oxides were uniaxially pressed up to 98 MPa, then milled and uniaxially pressed again up to 196 MPa. In this way, the air trapped inside the powders was eliminated. Preliminary sintering tests were performed with the disks in order to meet the conditions necessary to achieve densifications above 95%. Samples 10Fe and 20Fe reached 95% after being calcined at 1400 °C during 4 h. On the other hand, sample 0Fe only reached 90% densification after calcination at 1600 °C during 4 h. After the sintering process, disk morphologies were observed by SEM images.

Total conductivity measurements

Total conductivity was measured by Electrochemical Impedance Spectroscopy (EIS, Solartron 1260, UK). As current collector a thin layer of Pt-ink (Metalor) was deposited on each side of the sintered pellets and then calcined at 900 °C for 30 min. Impedance spectra were collected in the 0.1 Hz to 1 MHz frequency range, with an AC signal of 50–100 mV, in atmospheric air, at isothermal conditions, in the 150–850 °C temperature range. Each measurement was performed after reaching a stable temperature. The dependence of conductivity with temperature was fitted with the Arrhenius equation:

$$\sigma = \frac{\sigma_0}{T}\exp\left(-\frac{E_a}{RT}\right) \quad (2)$$

where σ is the conductivity, E_a is the activation energy, T is the absolute temperature and R is the universal gas constant.

Results and discussion

Characterization

Fig. 1(a) presents the XPD patterns of the three samples. All peaks can be assigned to the cubic fluorite structure of cerium dioxide; no additional peaks were observed. The position of the Bragg peaks slightly shifts to higher 2θ angles as the iron content grows, indicating the contraction of the unit cell. This shift can be observed in the 2θ region corresponding to Bragg peak (111) presented in Fig. 1(b). With the increasing concentration of iron the peaks become wider indicating that the crystallite size diminishes. It is important to remark that XRD Bragg peaks are symmetrical indicating homogeneity in composition.

The results of the Rietveld refinement are summarized In Table 1. The lattice parameter diminishes with increasing iron content. Many authors [22,23,27,28] attributed this shrinkage of the cerium oxide lattice to the substitution of the Ce^{4+} cation (0.097 nm) by the smaller Fe^{3+} cation (0.078 nm) [29]. Li et al. [23] and Zhu et al. [30] observed the decay in the lattice parameter at iron concentrations of 20 at.% and 10 at.%, respectively, and the segregation of a second phase of α-Fe_2O_3.

Kim [31] proposed an experimental equation to predict the variation of ceria lattice parameter (see Eq. (3)).

$$a = 0.5413 + \sum_k (0.0220\Delta r_k + 0.00015\Delta z_k)m_k \quad (3)$$

where "a" (nm) is the lattice parameter of ceria mixed oxide at room temperature, Δr_k (nm) is the difference in ionic radius between the kth dopant and the Ce^{4+} host cations, in eightfold coordination, Δz_k is the valence difference ($z_k - 4$), and m_k is the molar percentage of the k_{th} oxide incorporated in the ceria structure.

In Fig. 2, lattice parameters determined by Rietveld refinement and those predicted by Kim's equation for doped ceria samples are plotted together as a function of the iron atomic percentage. All lattice parameters are much higher than those predicted by Kim's equation as it would be expected for nano-sized crystallites [32].

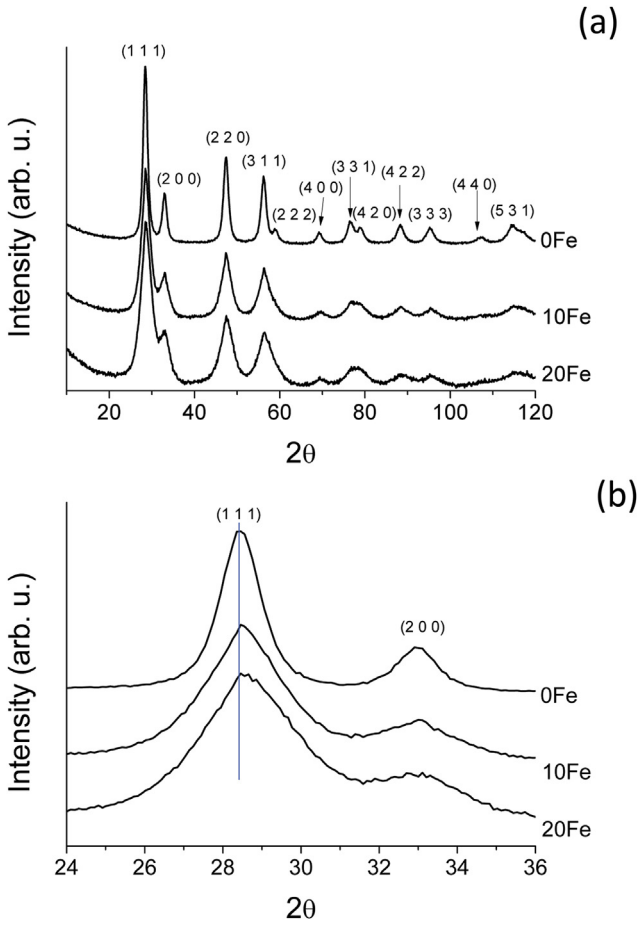

Fig. 1 – (a) XRD patterns of the three samples; (b) Expansion of the 2θ region corresponding to Bragg peaks (111) and (2 0 0).

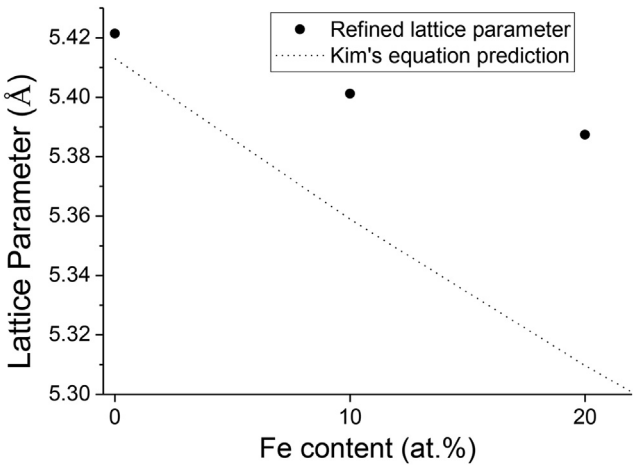

Fig. 2 – Plot of lattice parameter obtained from Rietveld refinement of XPD patterns and Kims' predicted values as a function of iron content.

Table 1 shows that crystallite size is influenced by iron content. Comparing with pure ceria it is possible to observe that a doping level of 10 and 20 at.% reduces crystallite size in 43% and 67%, respectively. The crystallite sizes reported here are among the smaller reported in the literature [23,27,28,30,33]. The very low crystallite size helps to stabilize the iron in the structure much above the solubility limit.

SEM images are presented in Fig. 3. It is possible to see a large amount of pores with no visible differences in the pore structure for the three samples. In addition, the particles looked agglomerated in accordance with the high agglomeration ratio estimated from physisorption measurements (Table 1). EDS chemical analysis was performed in different regions and the compositions obtained were consistent with the nominal values.

The TEM, HRTEM images, Selected Area Electron Diffraction patterns (SAEDs) and particle size histograms for the three samples are presented in Fig. 4. The SAEDs were recorded for areas containing a large number of particles. The concentric rings observed in these patterns are the result of the diffraction coming from a large number of small crystallites in all possible orientations. The rings are becoming continuous when iron content increases to 20 at.% indicating the nano-crystallinity of this sample. It is possible to reach the same conclusion after analysing the histograms obtained from HRTEM images. The particle size distribution is narrower and has lower average values as iron content increases. EDS results obtained during SEM and HRTEM experiments are consistent with the nominal composition of each sample.

Fig. 5 shows the N_2 adsorption isotherms. The isotherms are type II according to the IUPAC classification [34]. This kind of isotherm corresponds to monolayer-multilayer adsorption schema. Table 1 contains the BET specific surface area (S_{BET}), the diameter of the equivalent spherical particle size (D_{BET}) and the agglomeration ratio (D_{BET}/D_{XRD}). The specific surface area duplicates its value when iron content goes from 0 to 10 at.%, but no further increment is observed in sample 20Fe.

Table 1 – Lattice parameter and χ^2 factor obtained from Rietveld refinement; crystallite sizes obtained from Scherrer equation (DXPD) and HRTEM (DHRTEM). In the latter case the number of particles considered is also informed as number N; BET specific surface area obtained from physisorption results (SBET); spherical particle diameter (DBET) and agglomeration ratio (DBET/DXPD).

Sample name	Lattice parameter (Å)	χ^2	D_{XPD} (nm)	D_{HRTEM} (nm)	S_{BET} ($m^2\ g^{-1}$)	$D_{BET} = 6.(\rho.S_{BET})^{-1}$ (nm)	D_{BET}/D_{XPD}
0Fe	5.421(5)	1.239	5.6	7.2 ± 2.4 (N = 100)	20	42	7.5
10Fe	5.401(2)	1.773	3.17	4.4 ± 2.0 (N = 136)	39	23	7.3
20Fe	5.387(4)	2.086	2.42	3.2 ± 0.5 (N = 88)	40	22	9

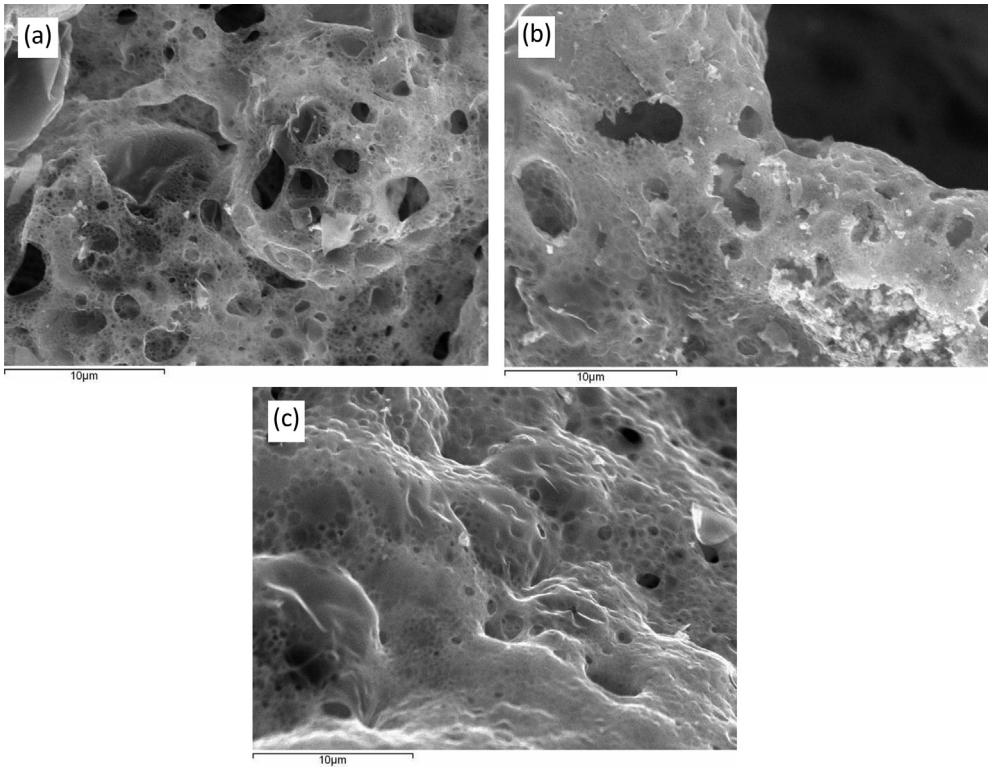

Fig. 3 – SEM images microscopies of (a) 0Fe, (b) 10Fe and (c) 20Fe.

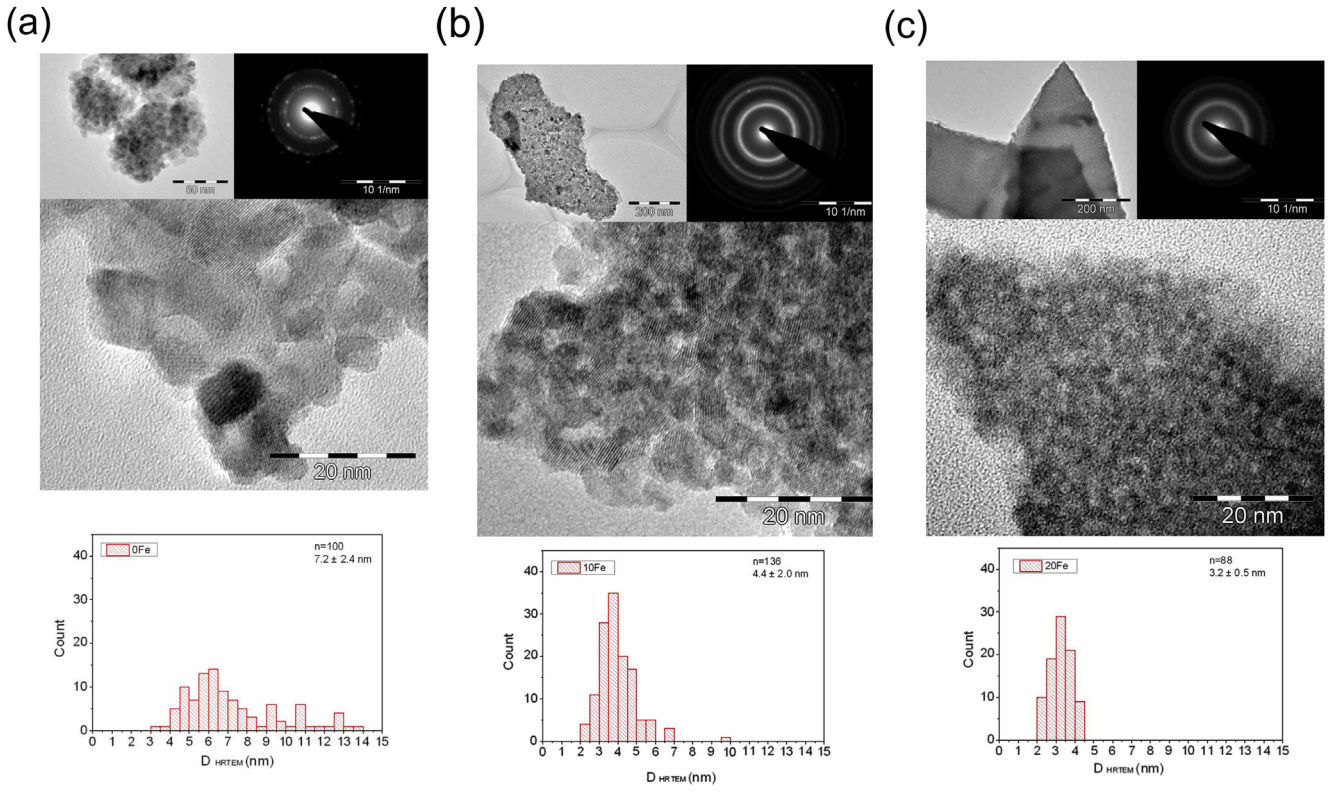

Fig. 4 – HRTEM high resolution images, particle size histograms and diffraction patterns for samples a) 0Fe; b) 10Fe and c) 20Fe.

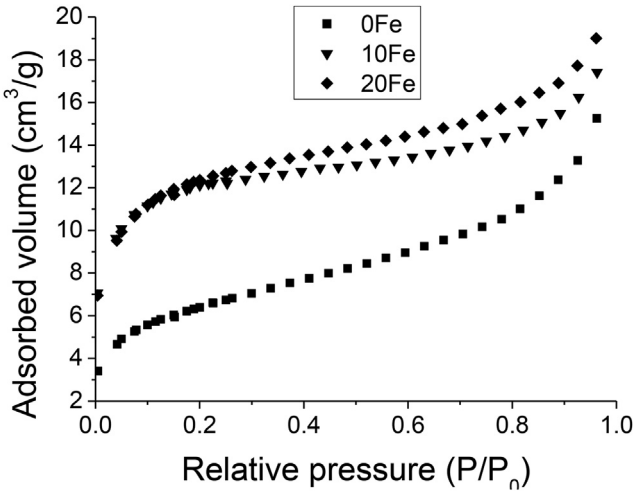

Fig. 5 – N_2 adsorption isotherms at (−196 °C).

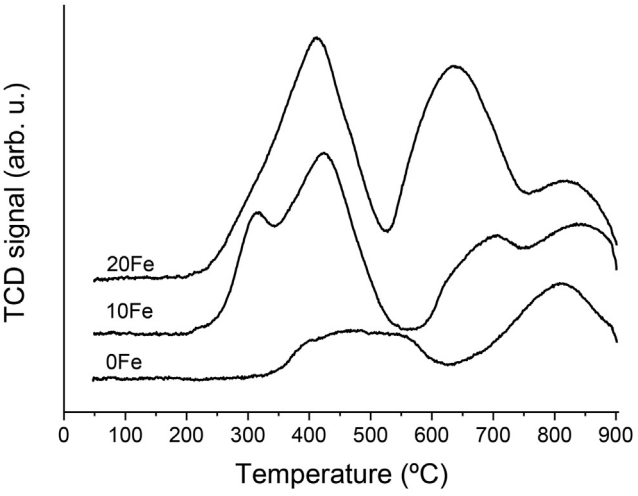

Fig. 6 – H_2-temperature programmed reduction (H_2-TPR) profiles.

The agglomeration ratio is quite high, with similar values in samples 0Fe and 10Fe (7.5 and 7.3, respectively) and slightly higher in sample 20Fe (9). These findings are in agreement with the SEM and TEM images shown in Figs. 3 and 4.

H_2-TPR profiles are presented in Fig. 6. Sample 0Fe, corresponding to pure ceria, shows two peaks. The first one corresponds to the reduction of surface cerium oxide and the second peak corresponds to the reduction of bulk cerium oxide [28]. There can be many different surface cerium atoms (cerium in pores and cerium on grain surface) that could be reduced through different reaction mechanisms. This can generate different reaction rates and make the first peak wider [35]. On the other hand, ferric oxide reduces in two or three steps as it is presented in the literature [28,36]. Laguna et al. [28] presented a two-step reduction process from Fe_2O_3 to Fe_3O_4 and then to Fe^0, while Zielinzki et al. [36] proposed an alternative reduction mechanism with the reduction of Fe_3O_4 to FeO and then to Fe^0.

The H_2-TPR patterns showed two extra peaks for sample 10Fe, which, according to hydrogen consumption, would correspond to the reduction of Fe^{3+} to $Fe^{2.33+}$. Sample 20Fe only shows an extra peak at 640 °C, but the first peak seems to be an overlapping of Fe^{3+} and surface cerium sites reduction. To confirm the species participating in the reduction process it would be necessary to perform "in situ" spectroscopy experiments. However, it is important to realize that both samples, 10Fe and 20Fe, started to reduce at lower temperatures (~200 °C in both cases) than the pure ceria (327 °C) and pure iron oxide (350 °C), indicating the beneficial effect of iron doping on the material reducibility. The temperatures of the reduction peaks and the reduction percentage calculated from hydrogen consumption and initial reducible species are summarized in Table 2. It is possible to see that sample 0Fe reached a lower reduction percentage (34%), while iron samples 10Fe and 20Fe reached 55% and 62%, respectively. These results indicate the easier reducibility of iron-doped samples. In applications as anodes of SOFCs, this feature positively contributes to the easy oxidation of fuel in the anode chamber.

Carbon dioxide is a weak acid molecule used to analyse the relative strength of basic sites on oxide surfaces. In our samples, carbon dioxide adsorption may take place through the interaction with oxygen anions (O^{2-}), to give carbonate structures, or oxygen vacancies, leading to the formation of carbonyl groups. Due to the fact that ceria is doped with an aliovalent cation (Fe^{3+}), it is expected an increasing number of oxygen vacancies with the increment in iron doping, causing an increase in CO_2 adsorption.

In Fig. 7 the CO_2-TPD results are shown. All powders present two peaks. The peak temperature is related to the strength of the corresponding basic site associated with the desorption process. If CO_2 is desorbed at lower temperature, the sites are weaker [37]. In our samples, the first peak is located at the same temperature (102 °C) for the three compositions. This peak is associated to the presence of weak basic sites probably related with oxygen ions of the ceria structure. On the other hand, the second peak is located at different temperatures for the three compositions. For samples 0Fe and 10Fe it is located at 452 °C, while for sample 20Fe

Table 2 – Temperature of peaks maxima in H_2-TPR profiles; percentage of reduction achieved at the end of H_2-TPR experiments; mmol of CO_2 desorbed per gram of powder in CO_2-TPD experiments.

Sample	T Peak 1 (°C)	T Peak 2 (°C)	T Peak 3 (°C)	T Peak 4 (°C)	Reduction percentage	CO_2 desorbed (mmol/g)
0Fe	400–570	813	–	–	34	0.60
10Fe	305	425	705	840	55	0.78
20Fe	420	640	820	–	62	0.91

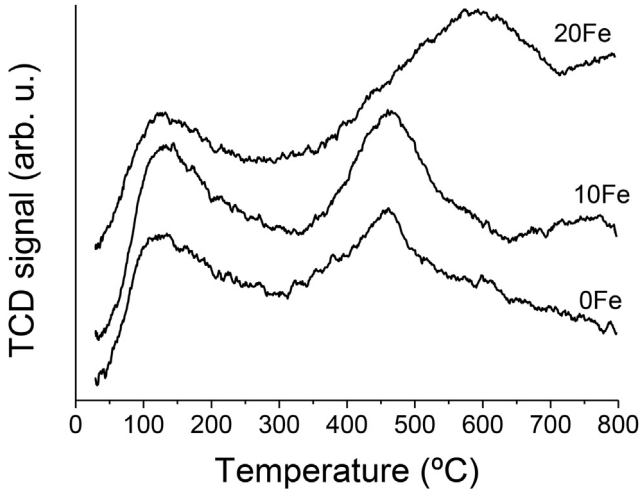

Fig. 7 – CO_2-temperature programmed desorption (CO_2-TPD) profiles.

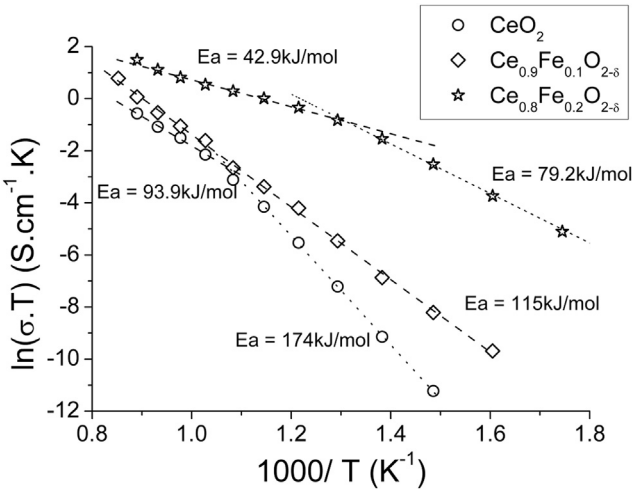

Fig. 9 – Arrhenius plot of total conductivity dependence with temperature.

it is at 602 °C. In the latter case, the signal is broad, starting at 327 °C and vanishing at 730 °C, indicating the presence of adsorption sites of higher strength.

Table 2 lists the amount of CO_2 desorbed in CO_2-TPD experiments. The large amount of CO_2 desorbed by sample 20Fe explains the prevalent basic character of this sample. This feature could prevent the formation of carbonaceous residues in the anode chamber of intermediate temperature SOFCs operated with hydrocarbons.

Total conductivity measurements

The micrographies of the sintered disks used in total conductivity measurements are shown in Fig. 8. Sample 0Fe has approximately 35 μm mostly uniform grain sizes. Samples 10Fe and 20Fe have a wider range of grain sizes with average values of 30 and 18 μm, respectively. The sample 20Fe has the smaller grain sizes indicating that the incorporation of iron avoids grain size growth.

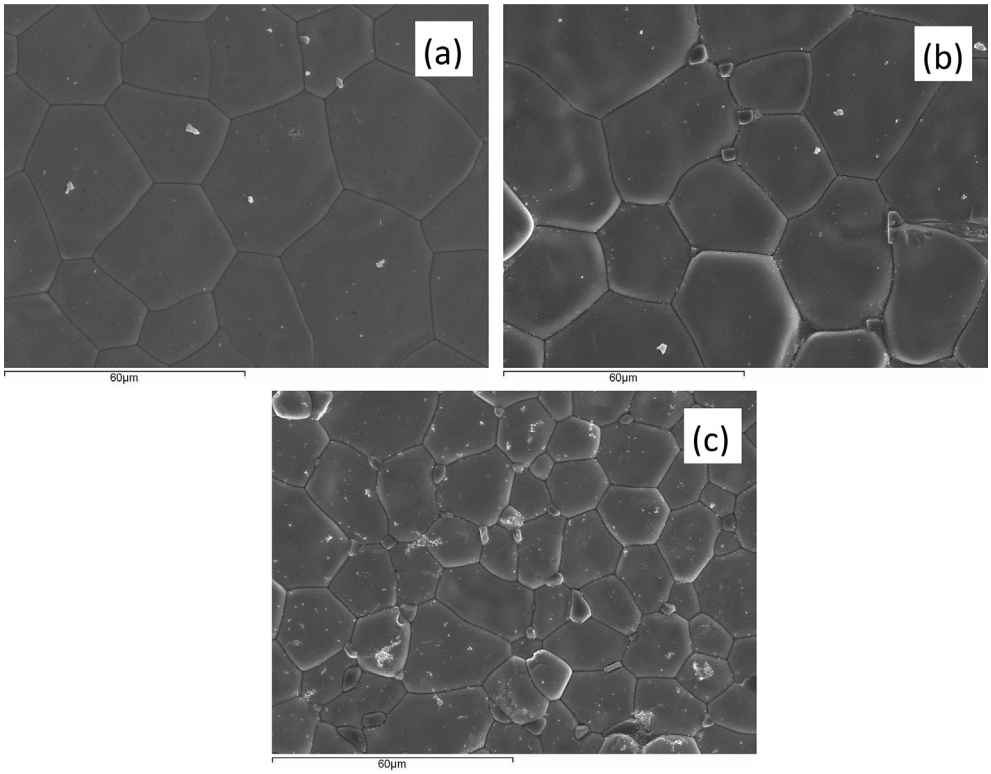

Fig. 8 – SEM images of sintered disks made of (a) 0Fe, (b) 10Fe and (c) 20Fe.

In Fig. 9, the typical Arrhenius plot of the dependence of total conductivity with temperature is presented. The substitution of cerium cations by iron cations improves total conductivity due to anionic vacancy formation and the presence of the Fe^{3+}/Fe^{2+} couple. A linear relation fits in case of sample 10Fe, as the Arrhenius equation predicts. For the other two samples two regions of linear relationship are observed: 150–600 °C and 700–800 °C for sample 0Fe and 150–450 °C and 500–800 °C for sample 20Fe.

Conclusions

Iron doped ceria was successfully synthesized through the freeze-drying method. All the solids were nanocrystalline. The incorporation of iron into the fluorite ceria structure reduces the crystallite size and the lattice parameter, increases the specific surface area and favours the sintering of the solid, which could be achieved at lower temperatures. Besides, the reducibility and the amount and strength of basic sites are also improved as well as the total conductivity.

All the above mentioned properties of iron doped ceria materials position them as promising materials for anodes of SOFCs operated with hydrogen o hydrocarbons.

Acknowledgements

A. Soldati acknowledges the valuable support of Dr. H. Troiani (CONICET, Metals Division, Bariloche Atomic Centre) in the TEM measurements.

Mr. Mazan and Mrs. Larrondo gratefully acknowledge the financial support by Vicerrectorados de Internacionalización y de Investigación de la Universidad de La Laguna 2013, respectively. Mr. Mazan PhD scholarship granted by FundaciónPeruilh, Facultad de Ingeniería, Universidad de Buenos Aires is also acknowledged.

The research work was supported by the financial contribution of projects MAT2010-16007 MINECO, Spain (Cofounded by FEDER); PIDDEF 2011-2013 N° 011/11, MINDEF, Argentina and Premio FOCA 2013, Galicia Sustentable.

REFERENCES

[1] British Petroleum. BP Statistical review of world energy 2014. www.bp.com.
[2] Singhal SC. Review solid oxide fuel cells for stationary, mobile, and military applications. Solid State Ionics 2003;152–153:405.
[3] Yamamoto O. Solid oxide fuel cells: fundamental aspects and prospects. Electrochim Acta 2000;45:2423.
[4] Boudghene Stambouli A, Traversa E. Solid oxide fuel cells (SOFCs): a review of an environmentally clean and efficient source of energy. Renew Sustain Energy Rev 2002;6:433.
[5] Minh NQ. Solid oxide fuel cell technology-features an applications. Solid State Ionics 2004;174:271.
[6] Lu C, An S, Worrell WL, Vohs JM, Gorte RJ. Development of intermediate-temperature solid oxide fuel cells for direct utilization of hydrocarbon fuels. Solid State Ionics 2004;175:47.
[7] Fergus JW. Oxide anode materials for solid oxide fuel cells. Solid State Ionics 2006;177:1529.
[8] [Chapter 12] Chatzichristodoulou Ch, Blennow PT, Søgaard M, Hendriksen PV, Mogensen MB. Ceria and its use in solid oxide cells and oxygen membranes in catalysis by ceria and related materials. In: Trovarelli A, editor. 2nd ed. 2013. p. 623.
[9] Fan L, Wan Ch, Chen M, Zhu B. Recent development of ceria-based (nano)composite materials for low temperature ceramic fuel cells and electrolyte-free fuel cells. J Power Sources 2013;234:154.
[10] Jacobson AJ. Materials for solid oxide fuel cells. Chem Mater 2010;22:660.
[11] Blennow P, Hansen KK, Wallenberg LR, Mogensen M. Electrochemical characterization and redox behavior of Nb-doped $SrTiO_3$. Solid State Ionics 2009;180:63.
[12] Marina OA, Bagger C, Primdahl S, Mogensen M. A solid oxide fuel cell with a gadolinia-doped ceria anode: preparation and performance. Solid State Ionics 1999;123:199.
[13] Marina OA, Mogensen M. High-temperature conversion of methane on a composite gadolinia-doped ceria–gold electrode. Appl Catal A 1999;189:117.
[14] Chourashiya MG, Jadhav LD. Synthesis and characterization of 10%Gd doped ceria (GDC) deposited on NiO-GDC anode-grade-ceramic substrate as half cell for IT-SOFC. Int J Hydrogen Energy 2011;36(22):14984.
[15] Fuentes RO, Baker RT. Synthesis and properties of Gadolinium-doped ceria solid solutions for IT-SOFC electrolytes. Int J Hydrogen Energy 2008;33(13):3480.
[16] Pérez-Alonso FJ, Melián-Cabrera I, López Granados M, Kapteijn K, Fierro JLG. Synergy of $Fe_xCe_{1-x}O_2$ mixed oxides for N_2O decomposition. J Catal 2006;239:340.
[17] Pérez-Alonso FJ, López Granados M, Ojeda M, Herranz T, Rojas S, Terreros P, et al. Relevance in the Fischer–Tropsch synthesis of the formation of Fe–O–Ce interactions on iron-cerium mixed oxide systems. J Phys Chem B 2006;110:23870.
[18] Pérez-Alonso FJ, Ojeda M, Herranz T, Rojas S, González-Carballo JM, Terreros P, et al. Carbon dioxide hydrogenation over Fe–Ce catalysts. Catal Commun 2008;9:1945.
[19] Lu XC, Zhu JH. Ni-Fe+SDC composite as anode material for intermediate temperature solid oxide fuel cell. Journal of Power Sources 2007;165:678.
[20] Lv H, Tu H, Zhano B, Wu Y, Hu K. Synthesis and electrochemical behavior of $Ce_{1-x}Fe_xO_{2-\delta}$ as a possible SOFC anode materials. Solid State Ionics 2007;177:3467.
[21] Lv H, Yang DJ, Pan X, Zheng J, Zhang C, Zhour W, et al. Performance of Ce/Fe oxide anodes for SOFC operating on methane fuel. Mater Res Bull 2009;44:1244.
[22] Li K, Wang H, Wei Y, Liu M. Preparation and characterization of $Ce_{1-x}Fe_xO_2$ complex oxides and its catalytic activity for methane selective oxidation. J Rare Earths 2008;26(1):245.
[23] Li K, Wang H, Wei Y, Yan D. Transformation of methane into synthesis gas using the redox property of Ce–Fe mixed oxides: effect of calcination temperature. Int J Hydrogen Energy 2011;36:3471.
[24] Zhao L, Bishop SR, Hyodo J, Ishihara T, Sasaki K. XRD and Raman spectroscopy study of Fe solubility in cerium oxide. ECS Trans 2013;50(40):53.
[25] Rodríguez-Carvajal J. FULLPROF: a program for rietveld refinement and pattern matching analysis. In: Satellite meeting on powder diffraction of the XV IUCr congress; 1990. p. 127.
[26] Cullity BD. Elements of X-ray diffraction. Reading, Massachussets, USA: Addison Wesley Publishng Company; 1956.
[27] Beausoleil II GL, Thurber A, Rao SS, Alanko GA, Hanna C, Punnoose A. Concentration dependence of magnetic moment in $Ce_{1-x}Fe_xO_2$. J Appl Phys 2012;111.

[28] Laguna OH, Centeno MA, Boutonnet M, Odriozola JA. Fe-doped ceria solids synthesized by the microemulsion method for CO oxidation reactions. Appl Catal B – Environ 2011;106:621.
[29] Shannon RD, Prewitt CT. Effective ionic radii in oxides and fluorides. Acta Crystallogr 1969;B25:925.
[30] Zhu X, Wei Y, Wang H, Li K. Ce–Fe oxygen carriers for chemical-looping steam methane reforming. Int J Hydrogen Energy 2013;38:4492.
[31] Kim DJ. Lattice parameters, ionic conductivities and solubility limits in fluorite-structure MO_2 oxide (M = $Hf4^+$, $Zr4^+$, Ce4+, Th4+, U4+) solid solutions. J Am Ceram Soc 1989;72(8):1415.
[32] Baranchikov AE, Polezhaeva OS, Ivanov VK, Tretyakov YD. Lattice expansion and oxygen non-stoichiometry of nanocrystalline ceria. Cryst Eng Comm 2010;12:3531.
[33] Zhang Z, Han D, Wei S, Zhang Y. Determination of active sites densities and mechanisms for soot combustion with O_2 on Fe-doped CeO_2 mixed oxides. J Catal 2010;276:16.
[34] Sing KSW, Everett DH, Haul RAW, Moscou L, Pierotti RA, Roquérol y J, et al. Reporting physisorption data for gas/solid systems with special reference to the determination of surface area and porosity. Pure Appl Chem 1985;57:603.
[35] Neri G, Pistone A, Milone C, Galvagno S. Wet air oxidation of p-coumaric acid over promoted ceria catalysts. Appl Catal B – Environ 2002;38:321.
[36] Zielinski J, Zglinicka I, Znak L, Kaszkur Z. Reduction of Fe_2O_3 with hydrogen. Appl Catal A – Gen 2010;381:191.
[37] Kamimura Y, Sato S, Takahashi R, Sodesawa T, Akashi T. Synthesis of 3-pentanone from 1-propanol over CeO_2–Fe_2O_3 catalysts. Appl Catal A – Gen 2003;252:399.